

Pushing and pulling on OH⁻ and H₃O⁺ with electric fields across water's surface

Kamal K. Ray^{‡1}, Aditya Limaye^{‡2}, Ka Chon Ng¹, Ankur Saha¹, Sucheol Shin³, Marie-Pierre Gaigeot⁴, Simone Pezzotti⁵, Adam P. Willard^{*2}, and Heather C. Allen^{*1}

¹ The Ohio State University, Department of Chemistry and Biochemistry, Columbus, OH 43210.

² MIT, Department of Chemistry, Cambridge, MA 02139.

³ University of Texas at Austin, Department of Chemistry, Austin, TX 78712.

⁴ Université Paris-Saclay, Univ Evry, CNRS, LAMBE UMR8587, 91025 Evry-Courcouronnes, France

⁵ Ruhr University Bochum, Department of Physical Chemistry II, D-44801 Bochum, Germany

*allen@chemistry.ohio-state.edu

*awillard@mit.edu

We use second harmonic generation (SHG) spectroscopy, molecular dynamics simulation, and theoretical modeling to study the response of the neat liquid water-air interface to changes in the potential of an external electrode positioned above the liquid. We observe a parabolic dependence of second harmonic intensity on applied potential. This dependence is reminiscent of bulk-phase electric field induced second harmonic (EFISH) but more complicated because it combines the second-order response of the topmost water layer and the potential dependent response of the interfacial electrical double-layer. Based on the literature values for these contributions, we derive a physical interpretation of our measurements that reveals new insight into the response of the neat water interface to external electric fields. Specifically, we find that the net dipolar orientation of water molecules within the double-layer is primarily responsive to the internal fields generated by the excess surface concentrations of OH⁻ and H₃O⁺ that arise to screen the external potential. Notably, this interpretation implies that the orientational response of water dipoles at the interface can actually oppose the direction of the external field, a subtle effect that is not captured by traditional models.

The physical, chemical, and biological properties of the liquid water-air interface are connected to, yet distinct from, those of the bulk liquid. These connections and distinctions must be characterized before we can fully understand the wide range of fundamental processes that are known to occur preferentially, or even exclusively, at the liquid water-air interface. In its most prevalent role - that of a solvent - water's properties are determined by the nanoscale structure and dynamics of the molecular hydrogen bonding network.¹⁻⁴ At an interface, this network is constrained and distorted, leading to anisotropy in the orientational distributions of water molecules as well as the electrostatic and dielectric properties that these distributions determine.⁵⁻¹⁰ Resolving the details of these interfacial properties is important because they have a significant influence on interfacial solvation and transport (especially for charged

species) as well as the thermodynamics and kinetics of aqueous interfacial chemical reactions, such as those that regulate the composition of our oceans and atmosphere, or the processes that control the assembly of supramolecular structures.¹¹⁻¹⁸

Over the last several decades, numerous scientific studies have been aimed at characterizing the molecular structure and associated electrostatic properties of the liquid water interface.¹⁹⁻²³ Despite these efforts, much remains to be understood about how the solvent properties of liquid water surfaces differ from those of the bulk and what those differences reveal about the interfacial molecular structure.²⁴⁻²⁸ Water surface properties are difficult to measure because common experimental probes cannot isolate the signal of the interface from that of the bulk, and those that can offer low signal to noise and/or report indirectly on the microscopic details of the surface. Furthermore, the interpretation of

interface-sensitive experiments is complicated by uncertainty in experimental probe-depth and limited reliability of theoretical models for treating interfacial systems.^{28, 29} Most notably, the various empirical force fields that are routinely used in molecular dynamics (MD) simulation, which are parameterized based on bulk properties, differ in their predictions of many key features of water's interfacial molecular structure.³⁰⁻³⁷

The molecular structure of the liquid water interface can be studied by measuring its polarization response under an applied electric field.³⁸⁻⁴³ Electric fields interact with the dipole moments of water molecules, biasing their orientational alignment. Second harmonic generation (SHG) spectroscopy is sensitive to the net interfacial dipole⁴⁴⁻⁴⁸ and can thus report upon the average molecular alignment of the water surface, the diffuse layer, and how these layers change under external fields. SHG has also been used to report hyperpolarizabilities of bulk materials using electric field induced SH (EFISH). By analyzing SHG changes and evaluating the data in the context of simple theoretical models, it is possible to gain information about the configurational statistics of interfacial water molecules and thereby infer details of interfacial molecular structure that are not apparent via unbiased measurement alone.

Results and discussion

Here we utilize SHG spectroscopy (SI, **Fig. S1**) to probe the response of the neat water-air interface to a tunable externally applied electric field, building upon the work of Schmid, Hurd, and Snavely.^{38, 42} The electric field is controlled by varying the potential of an electrode positioned in the air above a sample of neat liquid water; a second grounded electrode is directly below in the liquid (**Fig. 1A**). We observe a parabolic response such that the minimum intensity is offset to positive applied bias. We argue that changes in the overall SHG intensity under applied external potential (**Fig. 1B, 1C**) are due to subtle changes in the net dipole within the diffuse layer of the interface, *i.e.*, the region of net charge that is created by the diffusion of ions (H_3O^+ and OH^- in the case of neat water) along a potential gradient. The excess charge within the diffuse layer screens the external potential so that all static fields

are localized to the liquid interfaces and thus absent in the bulk.

We interpret the results of our experiments with a model of the water interface that includes water's second- and third-order susceptibilities, $\chi^{(2)}$ and $\chi^{(3)}$, respectively.^{29,49} In our model, described in more detail in the Theory section, the SHG intensity, I , is given by,

$$I \propto \left(\chi_{\text{TIL}}^{(2)} + \chi_{\text{DL}}^{(2)} \right)^2 \approx \left(\chi_{\text{TIL}}^{(2)} - \Phi_{\text{DL}} \chi_{\text{bulk}}^{(3)} \right)^2 \quad (1),$$

where $\chi_{\text{TIL}}^{(2)}$ denotes the second-order susceptibility of the topmost interfacial monolayer (TIL) of water molecules at the liquid water surface (analogous to the binding interfacial layer (BIL) at solid-liquid interfaces^{29,49}), and $\chi_{\text{DL}}^{(2)}$ is the second-order susceptibility of the diffuse layer that separates the TIL from the bulk liquid. The diffuse layer (DL) term varies with applied potential as reflected by the second equality in Eq. 1, where $\chi_{\text{bulk}}^{(3)}$ is the third-order susceptibility of the bulk liquid and Φ_{DL} denotes the potential drop across the DL. Here, we omit the wavevector dependent interference term that is often associated with the $\chi^{(3)}$ term (see Refs.⁴⁹⁻⁵³ for examples) based on the results of experiments carried out with dilute NaCl. These experiments (SI, **Fig. S2**) show minimal SHG intensity changes over differences in the DL width, indicating that interference effects can be neglected.

We assert that $\chi_{\text{TIL}}^{(2)}$ is constant over the range of fields we apply.^{8, 36} We base this assertion on the results of sum frequency generation (SFG) spectroscopy, which demonstrates a constant intensity of the dangling OH feature in the SFG spectrum as a function of applied potential (SI, **Figs. S3 – S5**). This implies that the molecular structure of the TIL water molecules remains unchanged with external potential. We note that in this interfacial system, the term $\chi_{\text{bulk}}^{(3)}$ is essentially an empirical parameter containing contributions from both nuclear and electronic reorientation of water molecules within the DL. In the case of water, the effects of nuclear reorientation are thought to dominate this parameter.^{54, 55}

We model the experimental results with Eq. 1 and assign the details of this model, using the literature value of $\chi_{\text{bulk}}^{(3)}$ for water.⁵⁰ We interpret our model

through a traditional theory of double-layer structure. Due to the effects of Boltzmann reweighing, the influence of an external potential (even at low or moderate strengths of ~ 1 -10V) causes concentrations of ions at the surface and within the DL to be enhanced by many orders of magnitude relative to those found in the bulk. The dipole field of the diffuse layer is thus subject to a combination of an external electric field, originating from the electrodes, and an internal electric field, originating from an excess concentration of OH^- or H_3O^+ (or any additional ionic species in solution) that are driven to the surface by the external field. Notably, the dipole field may also experience additional forces arising from the influence of these ions on interfacial hydrogen bonding network. In this way, Φ_{DL} of Eq. 1 represents an effective potential that combines these separate influences.

Because we are only concerned with electric fields perpendicular to the interface, we refer to the field as a single scalar resulting from dotting the electric field vector onto an interface normal pointing from the air side into the liquid water. Hence, a positive (or negative) field corresponds to the air electrode being held at a positive (or negative) potential relative to the grounded water electrode. The experimental results, plotted in **Fig. 1B**, reveal the response in SHG intensity, using a *pp* polarization combination, to positive and negative external potential (additional polarizations and control experiments are shown in **Figs. S6-S8**).

Based on Eq. 1, the parabolic shape of the SHG signal is the result of the $\chi_{DL}^{(2)}$ response. Second harmonic photons are generated from environments that lack centrosymmetry, such as the liquid-water interface.^{20, 45} The parabolic form of Eq. 1 presumes that changes in the net dipole of the DL scale linearly with applied field. The parabolic dependence of the data plotted in **Fig. 1B** thus confirms this presupposition. This linear response behavior suggests that the electric fields incident upon the water-air interface are not strong enough to significantly restructure the interfacial hydrogen bonding network of water; rather, they simply induce subtle changes in the orientational preference of molecules within the DL. This suggestion is supported by the results of molecular dynamics simulations (as described in more detail in the Methods section).

According to Eq. 1 and illustrated in **Fig. 1C**, the x-axis offset of the parabolic SHG intensity profile is determined by the relationship between $\chi_{TIL}^{(2)}$ and $\chi_{DL}^{(2)}$, and specifically is given by the ratio of $\chi_{TIL}^{(2)}/\chi_{bulk}^{(3)}$. Notably, EFISH contributions are also expected to exhibit a parabolic dependence of SHG intensity,⁵⁶ but this contribution is expected to be small compared to that arising from molecular reorientation.⁵⁴

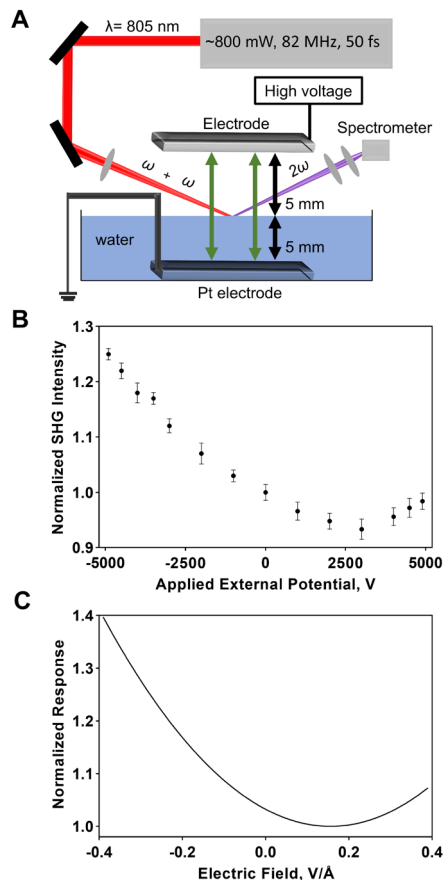


Figure 1. Probing the response of the water – air interface to an applied external potential. (A) Schematic diagram of the high voltage second harmonic generation set-up at the sample. The pulsed laser (Ti:sapphire, $\lambda = 805 \pm 10 \text{ nm}$, repetition rate 82 MHz , $< 50 \text{ fs}$, vertically polarized) generates the second order intensity that is detected (p-polarized). The high voltage set up is comprised of an air-phase electrode (DC-powered steel plate; $25 \text{ mm} \times 20 \text{ mm}$) and a grounded electrode in the condensed-phase (grounded parallel platinum plate; $25 \text{ mm} \times 22 \text{ mm}$). (B) Experimental normalized second harmonic generation intensity (sample signal divided by the reference signal at unbiased condition) with the externally applied electric potential of -5 kV to $+5 \text{ kV}$ revealing an intensity minimum at applied bias of approximately $+2.8 \text{ kV}$. (C) Theoretical model of the normalized squared interfacial dipole and parameters extracted from literature (see Methods section).

Experimentally, we control the potential difference between the two electrodes, yet the SHG intensity is dependent on the resulting electric field incident across the water-air interface. Deriving the magnitude of this field requires a theoretical model based on specific physical assumptions. The average electrostatic potential varies in space along the direction separating the two electrodes, which sets the boundary conditions, as illustrated in **Fig. 2**. The average electric field at any point within the system is thus given by the potential gradient at that point.

We begin by considering a Gouy-Chapman model of the water-air interface,^{57, 58} in which the mobile OH^- and H_3O^+ ions in water screen the potential drop over microscopic lengths at the water-air and water-electrode interfaces, also illustrated in **Fig. 2**. Accounting for the screening effects of OH^- and H_3O^+ , we model the water region as an electrolyte

solution with a dielectric $\epsilon = 80$ and a screening length of 960 nm, as appropriate for the experimental pH and temperature. The potential profile that satisfies the constraints that (i) the overall potential drop is 2.8 kV and (ii) the bulk liquid is fully screened yields an estimated interfacial field strength of the order $\pm 10^{-4} \text{ V/\AA}$ (**Fig. 2C**). A simple scaling argument (see Methods) reveals that this magnitude of electric field is far lower than the natural scale of electric field fluctuations in the hydrogen bond network of water; hence, this field is not expected to cause any significant restructuring of the hydrogen bond network. This expectation is further corroborated by both MD simulation and our vibrational sum frequency generation spectra, under polarized conditions, that show negligible intensity differences in the OH dangling bond vibration nor changes in the hydrogen bonded OH stretching region under applied potentials (SI, **Figs S3-S5**).

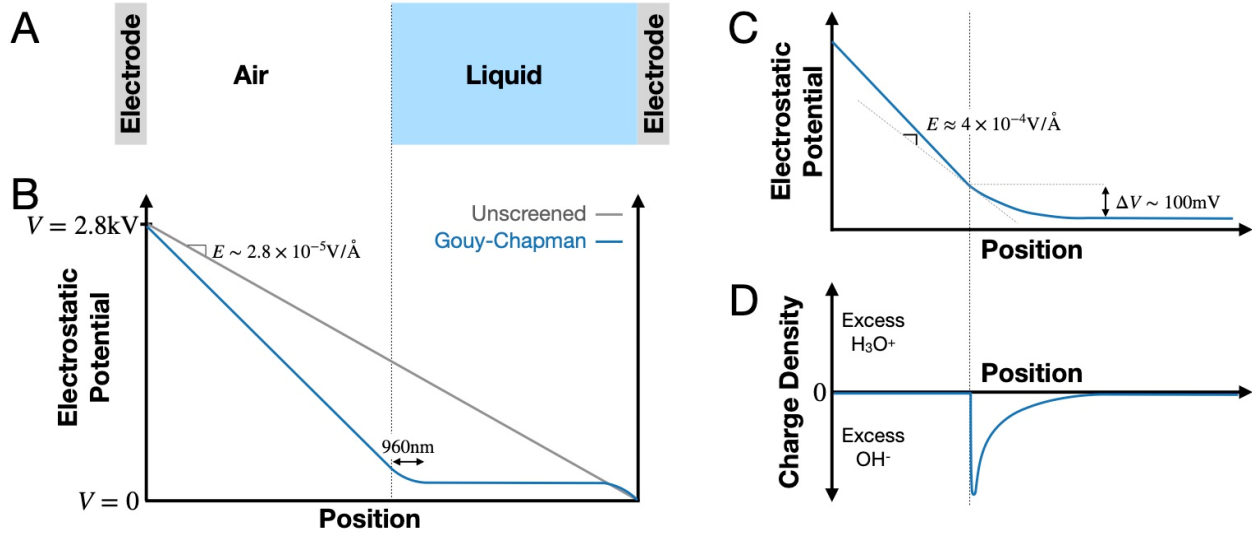


Fig. 2. Illustrating the Gouy-Chapman model as applied to the experimental setup. (A) A schematic of the experimental setup with a variable potential electrode on the left-hand side and a grounded ($V=0$) electrode on the right-hand side. (B) The formation of a screening layer at both liquid boundaries leads to an attenuation of the potential at the water interfaces, highlighted here at a potential of 2.8 kV. As indicated, the fields predicted in these screening regions are significantly larger than that originating from unscreened electrodes separated by vacuum (grey line). (C-D) An illustration of the potential profile and corresponding charge density profile at the water-air interface for positive applied potential. OH^- ions are drawn to the interface by the positive air electrode leading to a diffuse region of excess negative charge.

The position of the minimum in the parabolic SHG intensity profile reveals information about the fields that bias molecular orientation in the DL. We infer the directionality of these fields by fitting Eq.

1 to our experimental data. If we take $\chi_{bulk}^{(3)}$ from the literature⁵⁰, then the only fitting parameter is the value of the DL potential drop, Φ_{DL} . The result of this fitting procedure (see Methods for detail) is a

value of $\Phi_{DL} \approx -1.3$ mV. Remarkably, this effective potential carries the opposite sign of the externally applied potential.

We thus conclude that the orientations of water molecules within the DL are primarily responsive to the internal fields that originate from excess concentrations of OH^- or H_3O^+ , rather than from the average macroscopic fields that are predicted based on analysis of the average potential profile.

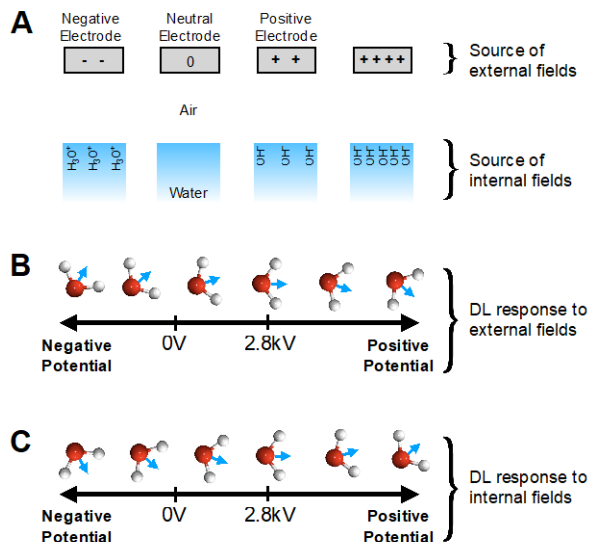


Figure 3. A. Illustrating the sources of external and internal electric fields. B. and C. The influence of internal and external fields on the dipole orientations of interfacial water molecules. Here, we associate the SHG intensity minimum with the state of zero net interfacial dipole.

To further contextualize our findings, we consider that the net electric field at any point within the liquid can be expressed as a sum of two components: an external field originating from the excess surface charge on the electrodes and an internal field originating from the excess OH^- and H_3O^+ that build up at the liquid interfaces (**Fig. 3**). These separate components act in opposite directions and completely cancel in the region of liquid between the two double-layers (i.e., the bulk). We propose here that the induced excess surface ion (e.g., hydroxide or hydronium) concentrations play the primary role in directing the dipoles of water molecules in the region of the interface.

At the SHG minimum at +2.8 kV, the positively charged electrode will drive the formation of an excess layer of OH^- at the liquid water-air interface and, as we propose, the fields from this excess will

affect the orientations of diffuse layer water molecules. The Gouy-Chapman model, illustrated in Fig. 2D, yields a rough estimate of the interfacial charge density required to screen the applied potential. At $V = 2.8$ kV the air-water interface holds a net charge density of $-8.1 \times 10^{-6} e \text{ nm}^{-2}$, corresponding to an ionic surface concentration of approximately 135 nM, or about 135 times $[\text{OH}^-]_{\text{bulk}}$ at pH=6. This surface concentration decays into the bulk with slope of 0.14 nM/nm.

An alternative approach for estimating ionic surface concentration is to determine the surface charge density required to achieve the value of the potential Φ_{DL} that we fit using Eq. 1. By construction, the surface charge density is equal to 0 when $V=0$. At the SHG intensity minimum of $V=2.8$ kV, $\rho_{\text{surf}} \approx 6$ nM. The 6 nM calculation includes implicit contributions of the electrode's opposing fields and therefore underestimates the actual surface charge concentration. Equation 1 also implies that this concentration varies linearly with applied potential with a slope of approximately 0.21 M/kV, transitioning to excess positive surface charges at negative applied potentials, as illustrated in Fig. 4. This analysis is further described in the Methods section (3.1.1).

Notably, these two approaches for estimating surface charge concentration yield different results (135 nM from GC and 6 nM from Eq. 1). The lack of consistency between the two calculations has several possible implications. First, the composition and structure of the liquid water interface under applied field is likely more complicated than it is assumed in Gouy-Chapman theory. For example, interfacial solvation thermodynamics can differ from the bulk and elevated concentrations can lead to correlations that are neglected in Gouy-Chapman theory. Second, within the roughly 960 nm diffuse layer the interfacial charge density profile attenuates giving rise to range of different local concentrations. Taking the maximum interfacial concentration, as we have done above, provides an upper bound on the effective operational value. Finally, the effective interfacial potential, Φ_{DL} , is an effective interfacial potential, and thus may combine competing effects from electrostatic, steric, and network forces. Consistency with SFG results would imply that interfacial concentrations are low enough to prevent changes to the interfacial hydrogen bonding network.

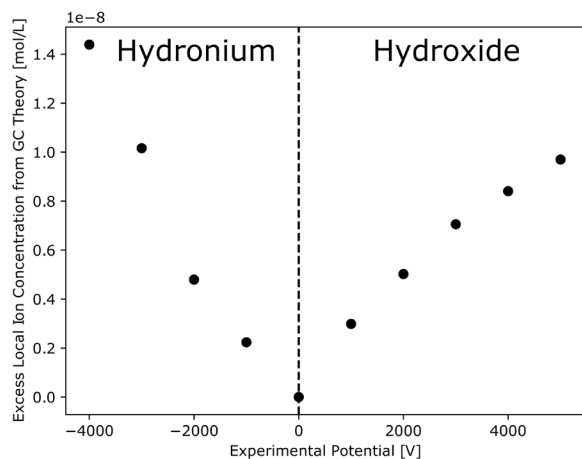


Figure 4. Excess local ion concentration derived from fitting Eq. 1 to experimental data. Here, excess refers to the concentration in addition to the bulk concentration. The calculated values are predicated on the assumption of zero excess local concentration at zero applied potential and a neutral pH.

The specific responsiveness of water's interfacial dipole to internal fields from interfacial concentrations of OH^- and H_3O^+ has an important physical implication. If our interpretation is correct, then interfacial internal fields that are relevant to molecular structure are not necessarily those predicted by traditional mean-field theories (e.g., Gouy-Chapman theory). In other words, the fields implied by the average potential profile cannot be applied to predict interfacial dipole properties. Further theoretical developments that identify the origins of these molecular effects and incorporate them into existing theoretical models are thus needed to advance our ability to interpret experimental data.

Conclusion

Our combined experimental and theoretical study reveals new insight into the molecular structure of the liquid water-air interface under ambient conditions, and how that structure is affected by the presence of external electric fields. Our experiments reveal a parabolic dependence of SHG intensity on applied field strength, with a minimum intensity at positive fields as generated by an external electrode held at a potential of 2.8kV relative to the ground. We interpret this parabolic profile with a model of

water's second harmonic response that includes a static second-order susceptibility arising from the surface layer of water molecules, and a potential dependent second-order susceptibility arising from the diffuse layer separating the surface and the bulk. Together, our experiments and modeling indicate that the molecular structure of the diffuse layer is primarily responsive to the internal fields arising from the excess surface OH^- and H_3O^+ that accumulate at the surface to screen the external potential. Within the bounds of the diffuse layer and responding to the internal fields generated from the OH^- and H_3O^+ , water molecules thus point in the opposite direction of the electric fields that arise from the externally applied potential.

Methods:

1.0 Materials and Sample Preparation

Milli-Q ($>18.0 \text{ M}\Omega$) ultra-pure water was used as a neat water source without the addition of any other chemicals. The purity of the neat water was confirmed by measuring the surface tension of water. Our measurements of $(72.15 \pm 0.08) \text{ mN/m}$ at $(23.1 \pm 0.5)^\circ\text{C}$ are in agreement with previous literature.^{59, 60} The pH was monitored; before the experiment, between 5-15 minutes after obtaining water from our Milli-Q system, the pH was measured to be 6.29 ± 0.05 at $(23.1 \pm 0.5)^\circ\text{C}$ (Table S1). The pH of water then dropped to (5.80 ± 0.08) after 5 to 6 hours of atmospheric exposure due to CO_2 absorption as is expected. Second harmonic measurement began 30 mins after obtaining the water samples from the Milli-Q system. Applied voltage experiments were completed over an ~5.5 to 6.5 hour time period in which sample height was adjusted to maintain alignment. The observed decrease of pH with time was shown to be undetectable by second harmonic measurement; reversing the order and randomization of experiments verified this conclusion, among other controls.

1.1 Second Harmonic Generation

1.1.1 Instrumentation and experimental set up. A lab-built Second Harmonic Generation system was utilized for these experiments (Fig. S1). The SHG

system consists of a Ti:sapphire oscillator (Tsunami, Spectra-Physics) with a wavelength centered at 805 nm, a half width half maximum of 10 nm, a sub 50 fs pulse width, and a repetition rate of 82MHz. The average output power from the Tsunami is around 860mW. The oscillator is pumped by a continuous wave (CW) solid state diode laser (Millennia Vs, Spectra-Physics) with a pump power of 5W. The output laser beam is separated by a ratio of 90/10 by a beam splitter, where 90% of the laser power is introduced to the sample channel and the other 10% of the beam is used in the reference channel (BBO nonlinear optical crystal). The sample channel consists of four dielectric mirrors (BB1-E03, Thorlabs), one Glan-laser polarizer (10GL08AR.16, Newport), one half-wave plate (10RP52-2B, Newport), one plano-convex lens with a focal length of 75mm (LA1608-B, Thorlabs) and one 690nm long-pass filter (690LP RapidEdge, Omega Optical). The laser pulses reflect off of the liquid surface with an angle of 67.2° with respect to the surface normal.

The detection system is comprised of a Czerny-Turner type monochromator (Shamrock SR303i, Andor Tech.) and an EMCCD (Newton DU970N-BV EMCCD, Andor Tech.). The monochromator grating is 68x68µm with a groove density of 300 lines/mm. The CCD consists of 1600x200 pixel array (Blazed at 500 nm), with 16x16 µm pixel size. Electron multiplying was set to 200 times to enhance the signal count and the thermal electric cooling was set at -60 °C to reduce thermal noise.

The high voltage set up is comprised of two electrodes: the DC-powered steel electrode (25x20 x0.40 mm³), located in the air-phase, and the grounded parallel platinum counter electrode (25x22x0.10 mm³, Fisher Scientific) in the condensed-phase. The applied external potential range was negative (-) 5 to positive (+) 5 kV, where the applied electric field was normal to the water-air interface. The distance between the air-phase electrode and the water surface was maintained at 5mm, whereas the condensed-phase electrode was maintained at 5mm below the water surface for fixed airgap experiments. The effect of the external potential on the water-air interface was also studied by changing the airgap between the water surface and the air-electrode from 5mm to 27mm with a constant external potential of +3 kV.

Note that additional details are discussed in the SI.

1.1.2 Data Normalization

Normalization of the second harmonic signal was done as a ratio of the reflected signal from the sample of interest to that of the neat water surface at zero applied potential (0 V and at P in P out polarization) noting that the neat water signal at P in P out polarization to itself is then defined as an intensity of unity.

1.1.3 Second Harmonic Intensity and Nonlinear Susceptibility. The second harmonic intensity of the water-air interface was collected using the lab built second harmonic instrument described above using pp polarization. (Other polarization data shown in the SI.) The reflected second harmonic signal intensity, $I(2\omega)$, on the neat water surface can be written in terms of the incoming laser intensity, $I(\omega)$, as follows:⁶¹⁻⁶³

$$I(2\omega) = \frac{32\pi^3\omega^2 \sec^2 \beta}{c_0^3 n_1(\omega) n_1(\omega) n_1(2\omega)} \left| \chi_{eff}^{(2)} \right|^2 I^2(\omega) \quad (1)$$

Where, c_0 , $n_i(\omega_i)$ and β denote the speed of light in vacuum, refractive index of the medium, and incident angle of the incoming laser normal to the water surface, respectively. Here, $\chi_{eff}^{(2)}$ indicates the effective second-order susceptibility of the water surface. The effective second-order susceptibility data of water at different external potentials and polarization are presented as Fresnel-removed second order susceptibilities in **Fig. S9** (Details in SI section 2 and 3).

The dependence of second harmonic signal intensity on surface potential and surface charges are well established and related to the bulk $\chi^{(3)}$.^{53-55, 64-66} This third-order contribution was first reported at the silica/water interface using second harmonic spectroscopy by Eienthal *et al.*.⁶⁴ EFISH predates this finding as a method for bulk $\chi^{(3)}$ determination.

2.1 Replicate and Control Experiments

2.1.1 Replicate Second Harmonic Measurements with Applied Potentials. Replicate measurements on water surface were performed under P in P out and 45 in S out polarization with the applied external potentials ranging from negative (-) 5 kV

to positive (+) 5 kV by keeping a fixed airgap of 5 mm (**Fig. S6** and **S7**). A minimum of six replicate measurements were performed for each data point presented. Here, we show six and two separate sets of experiments of P in P out and 45 in S out polarization data, respectively, to justify the robustness of the measurements. The measured data show higher and lower potential under negative and positive external potential, respectively, where the trends show similar behavior with the data presented in **Fig. 1B**. The measurements at individual external potential show highly reproducible data with negligible variation (~5% to 8%).

2.1.2 Applying a Fixed Potentials with Varying Airgap: Second Harmonic Response. The variation of the water surface second harmonic intensity was investigated under a fixed external potential (+3 and -3 kV) with varying airgaps ranging from 0.5 to 2.7 cm. The airgap was defined as the distance between the water surface and the air-electrode. We observe a monotonic decrease in experimental signal intensity with increasing separation distance between the air electrode and the water interface with an associated decrease in electric fields (**Fig. S8**).

3 Theory

3.1.1 TIL and DL Contributions. To explain the orientational distribution in terms of hyperpolarizabilities and to rule out interference / phase effects in our SHG measurements, we divide the interface into two sub-regions as previously discussed in the literature.²⁹ That is, the topmost interfacial layer (TIL), which has also been termed the Binding Interfacial Layer (BIL) in prior literature, composed by the topmost water molecules and hydrated ions at the surface, is followed by the Diffuse Layer (DL), where bulk-like water is reoriented by the static electric field present at the charged interface.^{29, 49, 50, 67} Both TIL and DL are SHG and SFG active, so the measured second order susceptibility $\chi^{(2)}$ is equal to:

$$\chi^{(2)} = \chi_{TIL}^{(2)} + \chi_{DL}^{(2)} \quad (2)$$

While the SHG activity of the TIL is due to its molecular structure, intrinsically different from the bulk, $\chi_{DL}^{(2)}$ intensity solely depends on the static

electric field across the interfacial DL region, and can be expressed for any charged aqueous interface via:^{49, 51, 52}

$$\chi_{DL}^{(2)} = \chi_{bulk}^{(3)} \int_{TIL/DL}^{\infty} E(z) e^{i\Delta K_z z} dz = -\chi_{bulk}^{(3)} \Phi_{DL} f(k \Delta K_z) \quad (3)$$

where the negative sign is used for consistency with the convention adopted in this work for the sign of the surface potential, and TIL/DL identify the boundary between the TIL and the DL region. $E(z)$ is the electric field at distance z from the surface, Φ_{DL} is the potential difference across the DL region and $f(k \Delta K_z)$ is the interference term, which depends on the wavevector mismatch (ΔK_z) and on the thickness of the interfacial region.⁵² $\chi_{DL}^{(2)}$ is hence a function of the response of bulk water ($\chi_{bulk}^{(3)}$) to the three fields: visible, infrared, and static electric field.^{29, 49, 50, 52, 67-69} The $\chi_{bulk}^{(3)}$ contribution has been shown to be dominated by water re-orientation processes and to be constant for various vapor-water and solid-water interfaces.^{29, 49, 50, 54, 55, 68-71}

The value of $\chi_{bulk}^{(3)}$ for SHG is $0.96 \cdot 10^{-21} \text{ m}^2/\text{V}^2$, as deduced in ref.⁵⁰. In our SHG experiments, the magnitude of the $f(k \Delta K_z)$ can be estimated by evaluating how the SHG intensity changes as a function of the ionic strength of the liquid solution (SI, **Fig. S2**). These experiments show that interference effects are negligible for the used experimental setup, so that we can simplify Eq. 3 to:

$$\chi^{(2)} = \chi_{TIL}^{(2)} - \chi_{bulk}^{(3)} \Phi_{DL} \quad (4)$$

Eq. 4 is used to fit the measured SHG intensity ($I(V) = |\chi^{(2)}|^2$) and extract Φ_{DL} , i. e. the potential difference across the liquid DL region. In the equation, $\chi_{bulk}^{(3)}$ is a known constant and the value of $\chi_{TIL}^{(2)}$ can be estimated from the SHG intensity measured at applied potential of 0V (where $\chi^{(2)} = \chi_{TIL}^{(2)}$ according to Eq. 4). A number of previous studies have shown that $\chi_{TIL}^{(2)}$ at the water-air interface only exhibits small changes with respect to concentration variations in pH and ions,^{8, 70, 72-74} while much larger variations are observed for $\chi_{DL}^{(2)}$. Because in our system we determine the SHG

intensity changes to be driven by accumulation of H_3O^+ and OH^- ions at the interface, we use the approximation of a constant $\chi_{TIL}^{(2)}$. As the measured SHG signal does not give information on the sign of $\chi^{(2)}$ ($I(V) = |\chi^{(2)}|^2$), the sign of $\chi_{TIL}^{(2)}$ can be assigned from the knowledge of the water dipole orientation within the TIL, as discussed in the text. $\chi_{TIL}^{(2)}$ has positive sign. Knowing this, we can also assign the sign of $\chi^{(2)}$ based on the following considerations.

The minimum SHG intensity is measured at positive applied potential of $V=2.8$ kV. This implies that:

- $\chi_{TIL}^{(2)}$ and $-\chi_{bulk}^{(3)} \Phi_{DL}$ add up for $V < 0V$.
- $\chi_{TIL}^{(2)}$ and $-\chi_{bulk}^{(3)} \Phi_{DL}$ compensate each other for $V > 0V$.

Therefore, $\chi^{(2)} = \sqrt{I(V)}$ has the same sign as $\chi_{TIL}^{(2)}$ for negative V values and changes sign at 2.8 kV:

$$\begin{aligned} &+\chi^{(2)}, & \text{if } V < 2.8 \text{ kV} \\ &-\chi^{(2)}, & \text{if } V > 2.8 \text{ kV} \end{aligned}$$

which gives:

$$\begin{aligned} \Phi_{DL} &= \frac{-\sqrt{I(V)} + \chi_{TIL}^{(2)}}{\chi_{bulk}^{(3)}} \text{ if } V < 2.8 \text{ kV} \\ \Phi_{DL} &= \frac{+\sqrt{I(V)} + \chi_{TIL}^{(2)}}{\chi_{bulk}^{(3)}} \text{ if } V > 2.8 \text{ kV} \end{aligned}$$

3.1.2 Gaussian Field Model. The characteristic feature of the experimental results in this system is a minimum in the spectroscopic response of the air-water interface at a non-zero applied field. Here, we sketch a simple Gaussian model for the interfacial polarization field that provides a compelling microscopic interpretation of the experimental result. It is known and well accepted that even under zero applied potential, water molecules at the air-water interface carry an intrinsic polarization due to broken longitudinal symmetry at the interface. To low order, we expect fluctuations

around the preferred polarization at any field to carry Gaussian statistics.

Equipped with these physical considerations, we postulate the following Hamiltonian for the z -component of the polarization variable π_z at the interface,

$$H[\pi_z] = \frac{k}{2} [\pi_z - \pi_z^*]^2 - \lambda \cdot \pi_z E_z$$

where π_z is the z -component (taken as normal to the interface by convention) of the plane-averaged dielectric polarization at the interface, π_z^* is the preferred value of the polarization at zero applied field, k is the energy scale associated with interfacial polarization fluctuations, E_z is the z -component of the applied interfacial electric field, and λ is a coupling constant quantifying the tendency of the applied electric field to align water dipoles at the interface. Mathematically, adding a linear coupling to a parabolic Hamiltonian simply translates the parabola to a new preferred polarization value. Completing the square results in an equivalent expression for the Hamiltonian that makes this field-dependent shift in the preferred polarization obvious,

$$H[\pi_z] = \frac{k}{2} \left[\pi_z - \left(\pi_z^* - \frac{\lambda E_z}{k} \right) \right]^2 - \lambda E_z \left(1 + \frac{\lambda E_z}{2k} \right).$$

At this point, we address units. For the sake of easily estimating parameters from molecular simulation, we track the polarization field π_z in fictive $\cos \theta$ units. One can glean the quantity in these units by normalizing the interfacial polarization vector by an arbitrary polarization scale, and then dotting the normalized vector into the interface normal. The Hamiltonian above is Gaussian, and so we can simply read off the mean from the offset in the quadratic term. Specifically, the mean polarization goes as,

$$\langle \pi_z \rangle = \pi_z^* - \frac{\lambda E_z}{k}$$

The spectroscopic response of the interface is proportional to the square of the mean interfacial polarization, plus any background signal,

$$\text{Response}[E_z] = B + A \cdot \langle \pi_z \rangle^2$$

where B is the magnitude of background signal, and A is a proportionality constant relating the interfacial polarization to the spectroscopic

response, both of which are assumed to be constant at all values of the applied interfacial field. Since the experimental data is normalized to the zero-field value, we can factor out the background response and eliminate it as an overall constant, leaving us with,

$$\text{NormResponse}[E_z] = 1 + \left(\frac{A}{B}\right) \cdot \left[\pi_z^* - \left(\frac{\lambda}{k}\right) E_z\right]^2$$

where the response carries a parametric dependence on the quantities π_z^* , λ/k , and A/B , which need to be estimated from simulation data.

First, the quantity $\langle\pi_z\rangle$ simply serves to scale the interfacial polarization into spectroscopic signal, and is assumed to be independent of the applied field. Since we can only access the value of $\langle\pi_z\rangle$ directly from simulation data, without loss of generality, we set $A/B = 1$. We choose to estimate the remaining model parameters, π_z^* , and λ/k using insight provided by simulations of an interface between water and a perfectly volume-excluding wall that can carry a surface charge. The surface charge density at the wall, σ_q , can be mapped to an effective interfacial electric field in the simulation data. **Fig. S10** shows a relationship between the surface charge density at the wall (measured in arbitrary units) vs. the computed interfacial electric field (in units of V/Å). The slope gleaned from this linear relationship is 0.65 V/Å, implying that the interfacial electric field increases by 0.65 V/Å for each σ_q unit.

As worked out in the section above on field magnitudes, the maximal applied experimental field is roughly 0.44 V/Å. Hence, simulations conducted with wall charge densities up to $\sigma_q \approx 0.68$ are in correspondence with the experimental field magnitudes. Trajectory analysis on the molecular dynamics simulation data allows for quantification of the orientational distributions of water molecules, resolved as a function of distance from the interface. **Fig. S11A** shows distributions of the interfacial polarization as a function of the wall charge density σ_q . **Fig. S11B** shows the modal value of the interfacial polarization as a function of σ_q . We choose to use the mode as a summary statistic for the distribution because it is more robust to the large tails of the distributions easily identifiable in **Fig. S11A**.

With the data in these two plots in hand, we estimate the values of the model parameters. The parameter λ/k describes how much the preferred polarization value moves with the applied interfacial field. If we employ the modal value of the $\cos\theta$ distribution as a proxy for the preferred polarization value and estimate the interfacial electric field in units of σ_q , then we can estimate λ/k from the data available in **Fig. S11B**. Specifically, λ/k is the slope of the response curve; we have a decision to make as to the range of σ_q values over which we fit this response slope. If we choose the dynamic range of $\sigma_q \in [-0.1, 0.1]$ for slope estimation from **Fig. S11B**, then we have $\lambda/k \approx 0.75$ in the aforementioned units. We can estimate the value of π_z^* , by examining the modal value of the interfacial polarization at zero externally applied field. Reading off the value at $\sigma_q = 0$ in **Fig. S11B** yields the estimate $\pi_z^* \approx 0.18$.

The typical length scale associated with the hydrogen bonding network of water is $L_{\text{scl}} = 1$ nm. Hence, by a simple scaling argument, the typical magnitude of electric field fluctuations associated with rearrangements of the hydrogen bond network is,

$$E_{\text{scl}} = \frac{k_B T}{e L_{\text{scl}}} \approx 2.5 \times 10^{-3} \frac{\text{V}}{\text{\AA}}.$$

3.1.3 Models for Experimental Field Magnitudes. In the experimental apparatus, the applied voltage between two parallel plates can reach as high as 5 kV. Naively, if we were to drop this entire voltage over the 5mm water layer as if in a parallel-plate capacitor, we would obtain a paltry (on a molecular scale) field of $E \approx 1 \times 10^{-4}$ V/Å. Insights from simulation data, and simple thermodynamic arguments (the field is far lower than the thermal field $E_{\text{thermal}} = k_B T / [e \times 1 \text{ \AA}]$) suggest that the field experienced at the interface is orders of magnitude greater than this simple parallel-plate capacitor argument may suggest.

We advance the hypothesis that elevated interfacial fields are present in the experiment due to formation of an electrical double-layer near the air-water interface by the hydronium and hydroxide ions present in water at the experimental pH. The

experiment is conducted at pH = 6.25, implying a hydronium concentration $c_{\text{Hydronium}} = 5.6 \times 10^{-7} \text{ mol/L}$ and a hydroxide concentration $c_{\text{Hydroxide}} = 5.6 \times 10^{-7} \text{ mol/L}$. The relevant length scale for formation of an electrical double layer is the Debye length,

$$\ell_{\text{Debye}} = \left[\frac{\epsilon k_B T}{\sum_j c_j q_j^2} \right]^{1/2}$$

where ϵ is the dielectric constant of neat water, k_B is the Boltzmann constant, T is the temperature, the sum runs over all ionic species j , and c_j and q_j denote the concentration and charge carried by the ionic species, respectively. At the experimental conditions, the Debye length is $\ell_{\text{Debye}} = 565 \text{ nm}$. If we assume that half the potential drop is dropped over the air-water double-layer (the other half is dropped over the grounded electrode-water double layer), then the maximal accessible interfacial field in experiment is roughly 0.44 V/\AA .

3.2 Molecular Dynamics Simulation Methods.

The molecular dynamics simulations employed in this work model water molecules using an atomistic molecular mechanics force field. The water molecules are in contact with an idealized wall of volume-excluding spheres carrying a constant surface charge, which is variable across different simulations. Orientational statistics of water molecules are computed relative to the local instantaneous interface, a construct developed by Willard and Chandler which factors out long-wavelength capillary wave-like fluctuations from the interface.⁷⁵ The distributions and values of order parameters from simulations presented in **Figs. S11A** and **S11B** are time averages taken over an entire trajectory of simulation.

Acknowledgments: “This work was supported by the U.S. Department of Energy, Office of Science, Basic Energy Sciences, under Awards # DE-SC0016381 and # DE-SC0018094, Allen and

Willard Labs, respectively. HCA and KKR acknowledge Prof. A. Co for helpful discussions.

Author contributions:

‡ KKR and AL contributed equally to this work. H.C.A, A.P.W., and K.K.R. conceived of the study and designed the experiments. K.K.R. and K.C.N. performed SHG setup. K.K.R. carried out SHG experiment, SHG characterization, and high voltage set up. A.L. performed calculations and MD simulations. A.S. and K.K.R. performed SFG characterization. H.C.A, A.P.W., A.L., and K.K.R. wrote the paper with help from all the authors.

Competing Interests

The authors declare no competing interests.

Additional information

Extended data is available for this paper at _____

Supplementary information is available for this paper at _...

Correspondence and requests for materials should be addressed to H.C.A and A.P.W. for experimental and theory detail, respectively.

Peer review information *Nature Communications* thanks the anonymous reviewers for their contribution to the peer review of this work.

Reprints and permissions information is available at ...

References

1. Ohmine, I.; Saito, S., Water Dynamics: Fluctuation, Relaxation, and Chemical Reactions in Hydrogen Bond Network Rearrangement. *Accounts of Chemical Research* **1999**, 32 (9), 741-749.
2. Ohmine, I.; Tanaka, H., Fluctuation, relaxations, and hydration in liquid water. Hydrogen-bond rearrangement dynamics. *Chem. Rev.* **1993**, 93 (7), 2545-66.
3. Smith, J. D.; Cappa, C. D.; Wilson, K. R.; Messer, B. M.; Cohen, R. C.; Saykally, R. J., Energetics of Hydrogen Bond Network

Rearrangements in Liquid Water. *Science* **2004**, *306* (5697), 851-853.

4. Nicodemus, R. A.; Corcelli, S. A.; Skinner, J. L.; Tokmakoff, A., Collective Hydrogen Bond Reorganization in Water Studied with Temperature-Dependent Ultrafast Infrared Spectroscopy. *J. Phys. Chem. B* **2011**, *115* (18), 5604-5616.

5. Jungwirth, P.; Finlayson-Pitts, B. J.; Tobias, D. J., Introduction: Structure and Chemistry at Aqueous Interfaces. *Chem. Rev.* **2006**, *106* (4), 1137-1139.

6. Goh, M. C.; Hicks, J. M.; Kemnitz, K.; Pinto, G. R.; Heinz, T. F.; Eienthal, K. B.; Bhattacharyya, K., Absolute orientation of water molecules at the neat water surface. *J. Phys. Chem.* **1988**, *92* (18), 5074-5.

7. Shen, Y. R.; Ostroverkhov, V., Sum-frequency vibrational spectroscopy on water interfaces: polar orientation of water molecules at interfaces. *Chem Rev* **2006**, *106* (4), 1140-54.

8. Gopalakrishnan, S.; Liu, D.; Allen, H. C.; Kuo, M.; Shultz, M. J., Vibrational spectroscopic studies of aqueous interfaces: salts, acids, bases, and nanodrops. *Chem Rev* **2006**, *106* (4), 1155-75.

9. Benjamin, I., Reaction dynamics at liquid interfaces. *Annu. Rev. Phys. Chem.* **2015**, *66*, 165-188.

10. Nihonyanagi, S.; Kusaka, R.; Inoue, K.-i.; Adhikari, A.; Yamaguchi, S.; Tahara, T., Accurate determination of complex $\chi(2)$ spectrum of the air/water interface. *J. Chem. Phys.* **2015**, *143* (12), 124707/1-124707/4.

11. Jungwirth, P.; Tobias, D. J., Surface effects on aqueous ionic solvation: A molecular dynamics simulation study of NaCl at the air/water interface from infinite dilution to saturation. *The Journal of Physical Chemistry B* **2000**, *104* (32), 7702-7706.

12. Benjamin, I., Theoretical study of ion solvation at the water liquid-vapor interface. *J. Chem. Phys.* **1991**, *95* (5), 3698-709.

13. Sitzmann, E. V.; Eienthal, K. B., Picosecond dynamics of a chemical reaction at

the air-water interface studied by surface second harmonic generation. *J. Phys. Chem.* **1988**, *92* (16), 4579-80.

14. McFearin, C. L.; Richmond, G. L., The Role of Interfacial Molecular Structure in the Adsorption of Ions at the Liquid-Liquid Interface. *J. Phys. Chem. C* **2009**, *113* (50), 21162-21168.

15. Garrett, B. C., Chemistry. Ions at the air/water interface. *Science* **2004**, *303* (5661), 1146-1147.

16. Culp, J. T.; Park, J.-H.; Stratakis, D.; Meisel, M. W.; Talham, D. R., Supramolecular Assembly at Interfaces: Formation of an Extended Two-Dimensional Coordinate Covalent Square Grid Network at the Air-Water Interface. *Journal of the American Chemical Society* **2002**, *124* (34), 10083-10090.

17. Kuzmenko, I.; Rapaport, H.; Kjaer, K.; Als-Nielsen, J.; Weissbuch, I.; Lahav, M.; Leiserowitz, L., Design and Characterization of Crystalline Thin Film Architectures at the Air-Liquid Interface: Simplicity to Complexity. *Chemical Reviews* **2001**, *101* (6), 1659-1696.

18. Neal, J. F.; Zhao, W.; Grooms, A. J.; Smeltzer, M. A.; Shook, B. M.; Flood, A. H.; Allen, H. C., Interfacial Supramolecular Structures of Amphiphilic Receptors Drive Aqueous Phosphate Recognition. *Journal of the American Chemical Society* **2019**, *141* (19), 7876-7886.

19. Conway, B. E.; Bockris, J. O. M.; Ammar, I. A., Dielectric constant of the solution in the diffuse and Helmholtz double layers at a charged interface in aqueous solution. *Trans. Faraday Soc.* **1951**, *47*, 756-66.

20. Benderskii, A.; Morita, A., Nonlinear spectroscopy and interfacial structure and dynamics. *J. Chem. Phys.* **2019**, *151* (15), 150401/1-150401/3.

21. Shiratori, K.; Morita, A., Molecular theory on dielectric constant at interfaces. A molecular dynamics study of the water/vapor

- interface. *J. Chem. Phys.* **2011**, *134* (23), 234705/1-234705/10.
22. Fumagalli, L.; Hu, S.; Ares, P.; Janardanan, A.; Yang, Q.; Radha, B.; Novoselov, K. S.; Geim, A. K.; Esfandiar, A.; Fabregas, R.; Gomila, G.; Taniguchi, T.; Watanabe, K., Anomalous low dielectric constant of confined water. *Science* **2018**, *360* (6395), 1339-1342.
 23. Dinpajooh, M.; Matyushov, D. V., Dielectric constant of water in the interface. *J Chem Phys* **2016**, *145* (1), 014504.
 24. Medders, G. R.; Paesani, F., Dissecting the Molecular Structure of the Air/Water Interface from Quantum Simulations of the Sum-Frequency Generation Spectrum. *J. Am. Chem. Soc.* **2016**, *138* (11), 3912-3919.
 25. Poli, E.; Jong, K. H.; Hassanali, A., Charge transfer as a ubiquitous mechanism in determining the negative charge at hydrophobic interfaces. *Nat. Commun.* **2020**, *11* (1), 901.
 26. Stipokin, I. V.; Weeraman, C.; Pieniazek, P. A.; Shalhout, F. Y.; Skinner, J. L.; Benderskii, A. V., Hydrogen bonding at the water surface revealed by isotopic dilution spectroscopy. *Nature* **2011**, *474* (7350), 192-195.
 27. Ohno, P. E.; Wang, H.-f.; Paesani, F.; Skinner, J. L.; Geiger, F. M., Second-Order Vibrational Lineshapes from the Air/Water Interface. *J. Phys. Chem. A* **2018**, *122* (18), 4457-4464.
 28. Reddy, S. K.; Thiriaux, R.; Wellen Rudd, B. A.; Lin, L.; Adel, T.; Joutsuka, T.; Geiger, F. M.; Allen, H. C.; Morita, A.; Paesani, F., Bulk Contributions Modulate the Sum-Frequency Generation Spectra of Water on Model Sea-Spray Aerosols. *Chem* **2018**, *4* (7), 1629-1644.
 29. Pezzotti, S.; Galimberti, D. R.; Shen, Y. R.; Gaigneot, M.-P., Structural definition of the BIL and DL: A new universal methodology to rationalize non-linear $\chi^{(2)}(\omega)$ SFG signals at charged interfaces, including $\chi^{(3)}(\omega)$ contributions. *Physical Chemistry Chemical Physics* **2018**, *20* (7), 5190-5199.
 30. Fan, Y.; Chen, X.; Yang, L.; Cremer, P. S.; Gao, Y. Q., On the Structure of Water at the Aqueous/Air Interface. *The Journal of Physical Chemistry B* **2009**, *113* (34), 11672-11679.
 31. Kühne, T. D.; Pascal, T. A.; Kaxiras, E.; Jung, Y., New Insights into the Structure of the Vapor/Water Interface from Large-Scale First-Principles Simulations. *The Journal of Physical Chemistry Letters* **2011**, *2* (2), 105-113.
 32. Dang, L. X.; Chang, T.-M., Molecular dynamics study of water clusters, liquid, and liquid-vapor interface of water with many-body potentials. *J. Chem. Phys.* **1997**, *106* (19), 8149-8159.
 33. Chacon, E.; Tarazona, P.; Alejandre, J., The intrinsic structure of the water surface. *J. Chem. Phys.* **2006**, *125* (1), 014709/1-014709/10.
 34. Dang, L. X.; Chang, T.-M., Many-body interactions in liquid methanol and its liquid/vapor interface: A molecular dynamics study. *The Journal of chemical physics* **2003**, *119* (18), 9851-9857.
 35. Kuo, I. F. W.; Mundy, C. J., An ab initio molecular dynamics study of the aqueous liquid-vapor interface. *Science* **2004**, *303* (5658), 658-660.
 36. Backus, E. H. G.; Schaefer, J.; Bonn, M., Probing the Mineral-Water Interface with Nonlinear Optical Spectroscopy. *Angew. Chem., Int. Ed.* **2021**, *60* (19), 10482-10501.
 37. Tang, F.; Ohto, T.; Sun, S.; Rouxel, J. R.; Imoto, S.; Backus, E. H. G.; Mukamel, S.; Bonn, M.; Nagata, Y., Molecular Structure and Modeling of Water–Air and Ice–Air Interfaces Monitored by Sum-Frequency Generation. *Chemical Reviews* **2020**, *120* (8), 3633-3667.
 38. Schmid, G. M.; Hurd, R. M.; Snavely, E. S., Jr., Effects of electrostatic fields on the surface tension of salt solutions. *J. Electrochem. Soc.* **1962**, *109*, 852-8.

39. Hayes, C. F., Water-air interface in the presence of an applied electric field. *J. Phys. Chem.* **1975**, *79* (16), 1689-93.
40. Pethica, B. A., Electric Field Effects on Air/Solution Interfaces. *Langmuir* **1998**, *14* (11), 3115-3117.
41. Jiang, Q.; Chiew, Y. C.; Valentini, J. E., Electric field effects on the surface tension of air/solution interfaces. *Colloids Surf., A* **1994**, *83* (2), 161-6.
42. Hurd, R. M.; Schmid, G. M.; Snavely, E. S., Jr., Electrostatic fields, their effect on the surface tension of aqueous salt solutions. *Science* **1962**, *135*, 791-2.
43. Laanait, N.; Mihaylov, M.; Hou, B.; Yu, H.; Vanysek, P.; Meron, M.; Lin, B.; Benjamin, I.; Schlossman, M., Tuning ion correlations at an electrified soft interface. *Proc. Natl. Acad. Sci. U. S. A.* **2012**, *109* (50), 20326-20331, S20326/1-S20326/6.
44. Wang, H.; Borguet, E.; Eienthal, K. B., Polarity of Liquid Interfaces by Second Harmonic Generation Spectroscopy. *J. Phys. Chem. A* **1997**, *101* (4), 713-718.
45. Shen, The principles of nonlinear optics. 1984.
46. Corn, R. M.; Higgins, D. A., Optical second harmonic generation as a probe of surface chemistry. *Chem. Rev.* **1994**, *94* (1), 107-25.
47. Zhao, X.; Ong, S.; Eienthal, K. B., Polarization of water molecules at a charged interface. Second harmonic studies of charged monolayers at the air/water interface. *Chem. Phys. Lett.* **1993**, *202* (6), 513-20.
48. Boyd, R. W., Nonlinear optics. **2003**.
49. Wen, Y.-C.; Zha, S.; Liu, X.; Yang, S.; Guo, P.; Shi, G.; Fang, H.; Shen, Y. R.; Tian, C., Unveiling Microscopic Structures of Charged Water Interfaces by Surface-Specific Vibrational Spectroscopy. *Physical Review Letters* **2016**, *116* (1), 016101.
50. Dalstein, L.; Chiang, K.-Y.; Wen, Y.-C., Direct Quantification of Water Surface Charge by Phase-Sensitive Second Harmonic Spectroscopy. *The Journal of Physical Chemistry Letters* **2019**, *10* (17), 5200-5205.
51. Ohno, P. E.; Wang, H.-f.; Geiger, F. M., Second-order spectral lineshapes from charged interfaces. *Nat. Commun.* **2017**, *8* (1), 1-9.
52. Gonella, G.; Lütgebaucks, C.; de Beer, A. G. F.; Roke, S., Second Harmonic and Sum-Frequency Generation from Aqueous Interfaces Is Modulated by Interference. *The Journal of Physical Chemistry C* **2016**, *120* (17), 9165-9173.
53. Geiger, F. M., Second harmonic generation, sum frequency generation, and χ (3): dissecting environmental interfaces with a nonlinear optical Swiss Army knife. *Annual review of physical chemistry* **2009**, *60*, 61-83.
54. Joutsuka, T.; Morita, A., Electrolyte and Temperature Effects on Third-Order Susceptibility in Sum-Frequency Generation Spectroscopy of Aqueous Salt Solutions. *J. Phys. Chem. C* **2018**, *122* (21), 11407-11413.
55. Joutsuka, T.; Hirano, T.; Sprik, M.; Morita, A., Effects of third-order susceptibility in sum frequency generation spectra: a molecular dynamics study in liquid water. *Physical Chemistry Chemical Physics* **2018**, *20* (5), 3040-3053.
56. Lee, C. H.; Chang, R. K.; Bloembergen, N., Nonlinear electroreflectance in silicon and silver. *Phys. Rev. Lett.* **1967**, *18* (5), 167-70.
57. Gouy, Constitution of the Electric Charge at the Surface of an Electrolyte. *J. physique, [4]* **1910**, *9*, 457-67.
58. Chapman, D. L., A contribution to the theory of electrocapillarity. *Philosophical Magazine* **1913**, *25* (6), 475-481.
59. Vargaftik, N. B.; Volkov, B. N.; Voljak, L. D., International tables of the surface tension of water. *Journal of Physical and Chemical Reference Data* **1983**, *12* (3), 817-820.
60. Berry, J. D.; Neeson, M. J.; Dagastine, R. R.; Chan, D. Y. C.; Tabor, R. F., Measurement of surface and interfacial

tension using pendant drop tensiometry.

Journal of colloid and interface science **2015**, 454, 226-237.

61. Rao, Y.; Tao, Y.-s.; Wang, H.-f., Quantitative analysis of orientational order in the molecular monolayer by surface second harmonic generation. *The Journal of chemical physics* **2003**, 119 (10), 5226-5236.

62. Zhuang, X.; Miranda, P. B.; Kim, D.; Shen, Y. R., Mapping molecular orientation and conformation at interfaces by surface nonlinear optics. *Physical Review B* **1999**, 59 (19), 12632.

63. Bian, H.-t.; Feng, R.-r.; Xu, Y.-y.; Guo, Y.; Wang, H.-f., Increased interfacial thickness of the NaF, NaCl and NaBr salt aqueous solutions probed with non-resonant surface second harmonic generation (SHG). *Phys. Chem. Chem. Phys.* **2008**, 10 (32), 4920-4931.

64. Ong, S.; Zhao, X.; Eienthal, K. B., Polarization of water molecules at a charged interface: second harmonic studies of the silica/water interface. *Chemical Physics Letters* **1992**, 191 (3-4), 327-335.

65. Yan, E. C. Y.; Liu, Y.; Eienthal, K. B., New method for determination of surface potential of microscopic particles by second harmonic generation. *The Journal of Physical Chemistry B* **1998**, 102 (33), 6331-6336.

66. Salafsky, J. S.; Eienthal, K. B., Protein adsorption at interfaces detected by second harmonic generation. *The Journal of Physical Chemistry B* **2000**, 104 (32), 7752-7755.

67. Urashima, S.-h.; Myalitsin, A.; Nihonyanagi, S.; Tahara, T., The Topmost Water Structure at a Charged Silica/Aqueous Interface Revealed by Heterodyne-Detected Vibrational Sum Frequency Generation Spectroscopy. *The Journal of Physical Chemistry Letters* **2018**, 9 (14), 4109-4114.

68. Saito, K.; Wang, L.; Joutsuka, T.; Morita, A.; Peng, Q.; Qiao, L.; Ye, S.; Ishiyama, T., Theoretical and experimental examination of SFG polarization analysis at

acetonitrile-water solution surfaces. *Phys Chem Chem Phys* **2017**, 19 (13), 8941-8961.

69. Wang, H.; Xu, Q.; Liu, Z.; Tang, Y.; Wei, G.; Shen, Y. R.; Liu, W.-T., Gate-Controlled Sum-Frequency Vibrational Spectroscopy for Probing Charged Oxide/Water Interfaces. *The Journal of Physical Chemistry Letters* **2019**, 10 (19), 5943-5948.

70. Pezzotti, S.; Gaigeot, M.-P., Spectroscopic BIL-SFG Invariance Hides the Chaotropic Effect of Protons at the Air-Water Interface. *Atmosphere* **2018**, 9 (10).

71. Pezzotti, S.; Galimberti, D. R.; Gaigeot, M.-P., Deconvolution of BIL-SFG and DL-SFG spectroscopic signals reveals order/disorder of water at the elusive aqueous silica interface. *Phys Chem Chem Phys* **2019**, 21 (40), 22188-22202.

72. Hua, W.; Verreault, D.; Allen, H. C., Relative Order of Sulfuric Acid, Bisulfate, Hydronium, and Cations at the Air-Water Interface. *Journal of the American Chemical Society* **2015**, 137 (43), 13920-13926.

73. Tian, C.; Ji, N.; Waychunas, G. A.; Shen, Y. R., Interfacial Structures of Acidic and Basic Aqueous Solutions. *Journal of the American Chemical Society* **2008**, 130 (39), 13033-13039.

74. Sun, S.; Schaefer, J.; Backus, E. H. G.; Bonn, M., How surface-specific is 2nd-order non-linear spectroscopy? *J. Chem. Phys.* **2019**, 151 (23), 230901/1-230901/7.

75. Willard, A. P.; Chandler, D., Instantaneous Liquid Interfaces. *The Journal of Physical Chemistry B* **2010**, 114 (5), 1954-1958.

Supplementary Information

Pushing and pulling on OH⁻ and H₃O⁺ with electric fields across water's surface

Kamal K. Ray¹, Aditya Limaye², Ka Chon Ng¹, Ankur Saha¹, Sucheol Shin³, Marie-Pierre Gageot⁴, Simone Pezzotti⁵, Adam P. Willard^{*2}, and Heather C. Allen^{*1}

¹ The Ohio State University, Department of Chemistry and Biochemistry, Columbus, OH 43210.

² MIT, Department of Chemistry, Cambridge, MA 02139.

³ University of Texas at Austin, Department of Chemistry, Austin, TX 78712.

⁴ Université Paris-Saclay, Univ Evry, CNRS, LAMBE UMR8587, 91025 Evry-Courcouronnes, France

⁵ Ruhr University Bochum, Department of Physical Chemistry II, D-44801 Bochum, Germany

*allen@chemistry.ohio-state.edu

*awillard@mit.edu

Table of Contents

1. Supplementary Figures: S1 to S11

2. Discussion of calculation of second harmonic generation power

3. Calculation of effective second order susceptibility $\chi_{eff}^{(2)}$

4. Supplementary Table S1 to S2

1. Supplementary Figures:

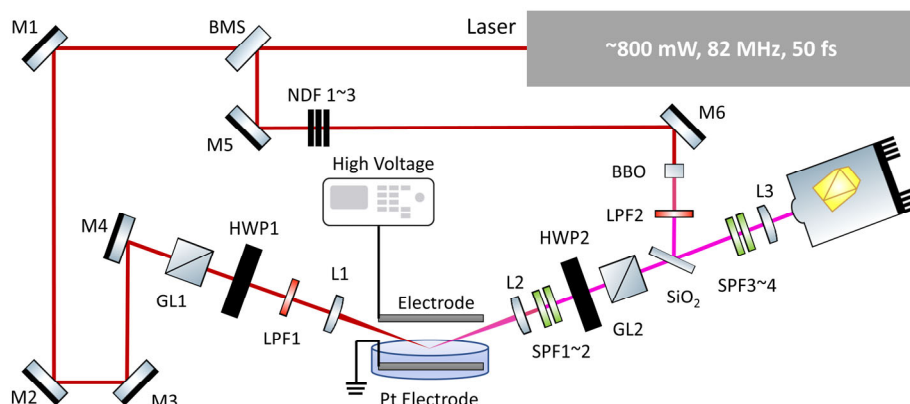


Fig. S1. The schematic of the custom built second harmonic generation spectroscopy instrument for the high voltage application to the water-air interface. A broadband Ti:sapphire laser has a frequency centered at 805 ± 10 nm with a sub 50 fs pulse width and a repetition rate of 82 MHz. The average power before exciting the sample was 550 mW. The interfacial second harmonic signal has a center wavelength of 403 nm, which is generated by the aqueous sample. The sample channel beam is focused by a 50 mm focusing lens (LA1131-B, Thorlabs) into the detector. The second harmonic instrument includes sample and reference channels that measure sample and reference intensity. Here, BMS, M (1,2,3,4,5 and 6), GL (1 and 2), LPF (1,2, 3 and 4), SPF (1,2,3 and 4), L (1,2), NDF (1,2,3), SiO₂ and BBO stands for beam splitter, mirror, Glan-laser polarizer, long pass filter, short pass filter, lens, neutral density filter, silica plate and α -BBO crystal, respectively. A polarizer, half-wave plate, and long-pass filter are used to purify the input and detected polarizations.

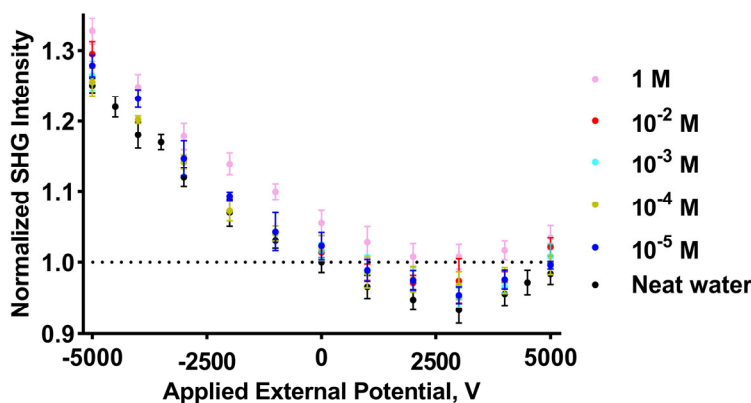


Fig. S2. Examining interference effects. The second harmonic intensities of NaCl solutions at different concentration and external potential are normalized with respect to the neat water intensity at zero external potential. Here, the pink, red, black, green, sky blue, yellow, and blue colors indicate the average second harmonic intensity with one standard deviation of the experiment 1, 10^{-2} , 10^{-3} , 10^{-4} and 10^{-5} M NaCl, respectively. The average second harmonic intensity of neat water are shown in black color to compare the intensity variation of NaCl with different concentrations.

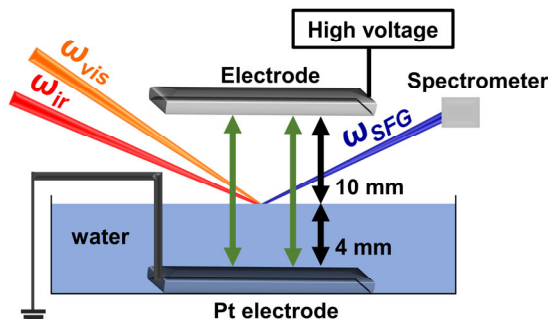


Fig. S3. Schematic diagram of the sum frequency generation experimental set-up for the high voltage application at the water-air interface. The visible (ω_{vis}) and IR (ω_{ir}) laser beams were focused on the sample. The sum frequency signal is collected in the reflected direction by a spectrometer (IsoPlane SCT 320, Princeton Instruments) and a liquid nitrogen cooled CCD (PyLoN, 1340×400 pixels, Princeton Instruments). The high voltage set up is comprised of an air-phase electrode (DC-powered steel plate in the range -5 kV to +5 kV) and a grounded platinum counter electrode in the condensed-phase. The sum frequency measurements were done with a typical gap of 10 mm and 4 mm between the water surface to the air electrode and Pt electrode, respectively. The details of the broadband sum frequency generation spectrometer set up used for this study were previously reported³⁻⁵. In brief, a regenerative Ti:sapphire amplifier (Spitfire Ace, Spectra-Physics) seeded with a sub-50 fs 800 nm pulse from a Ti:sapphire oscillator provides an ~ 3.5 W beam of 75 fs pulses and 1 kHz repetition rate. The amplified beam is then directed through a 50:50 beam splitter. One half of the beam is used to pump an optical parametric amplification system (TOPAS-C, Light Conversion), that is coupled to a non-collinear difference frequency generator (NDFG, Light Conversion) to generate the broadband infrared beam. The other half of the beam is spectrally narrowed to a FWHM of 12 cm^{-1} by an etalon (SLS Optics, United Kingdom) and is used as the visible 797 nm beam. The infrared and the visible beams are co-propagating and fall on the sample surface at angle from the surface normal of 60 and 50 degrees, respectively. The visible beam is focused approximately 1 cm after the surface with a BK7 lens (25 cm FL) and the infrared beam is focused on the sample surface with a CaF_2 lens (15 cm FL). The sum frequency signal is collected in the reflected direction by a spectrometer (IsoPlane SCT 320, Princeton Instruments) and a liquid nitrogen cooled CCD (PyLoN, 1340×400 pixels, Princeton Instruments). The IR laser profile and energies of visible and IR beam were periodically measured and was stable throughout the measurement. The polarization combinations used in the sum frequency experiments were ppp and ssp are listed in the order of decreasing frequency (SF, Vis, IR). Light polarized perpendicular to the incident plane is referred to as s polarized, whereas light polarized parallel to the incident plane is p polarized. The vibrational modes that contribute to a particular polarization combination depend on the polarization of the infrared field and the direction of the infrared and Raman transition moments. The ssp polarization combination accesses vibrational modes primarily with dipole transition moments that have components perpendicular to the surface plane. Whereas, vibrational modes with components that are both perpendicular and parallel to the surface plane will be present in ppp polarization.⁶

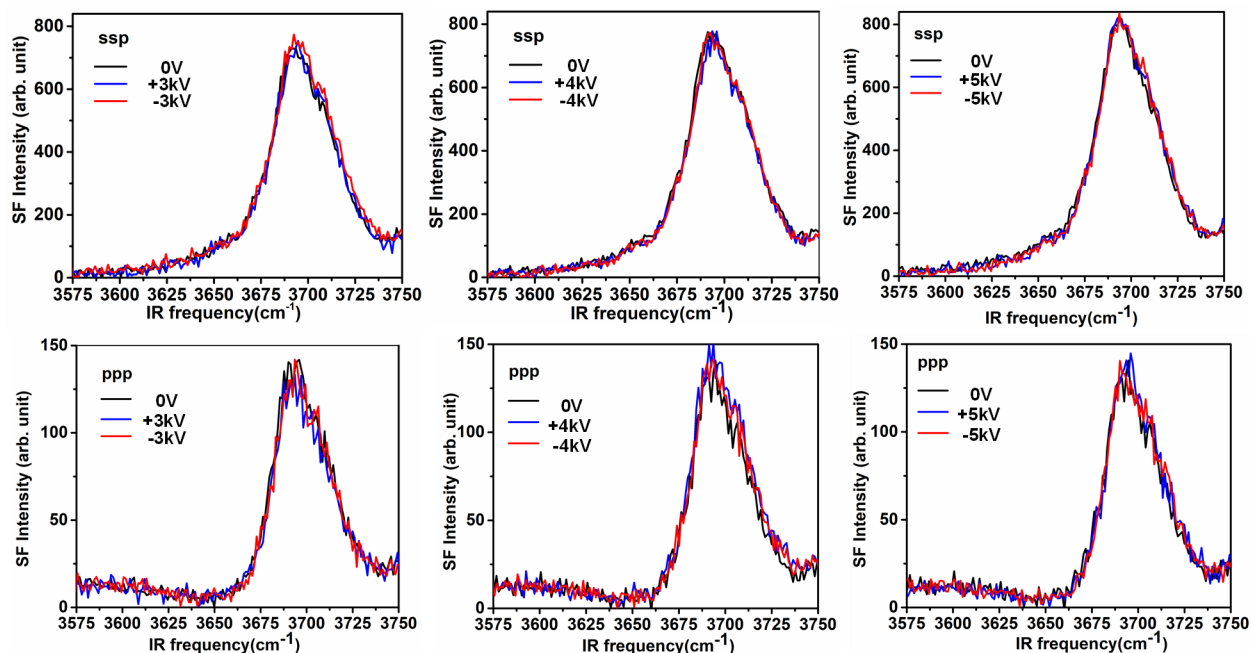


Fig. S4. The background subtracted vibrational sum frequency generation spectra of the neat water-air interface with ssp (upper panel) and ppp (lower panel) polarization combination under applied external potential. The spectral region covers 3575 -3750 cm^{-1} inclusive of the higher energy OH stretch region and the free (dangling) OH stretch of the water molecules that straddle the water-air interface. The polarizations are listed in the order of decreasing frequency from left to right (sum frequency, visible, IR). The black, blue, and red colors represent sum frequency spectra under unbiased (0 V), positive and negative applied potential, respectively. No change in intensity is noted from unbiased to applied potentials, and thus no orientational change of the free OH is detected (each plot should be compared within itself for intensity variations). The sum frequency spectra for the free OH spectral region were obtained with 20 sec integration time and 3 averages and plotted after background subtraction. The measured sum frequency spectra show no appreciable change under applied external potential in the range of negative (-) 5 kV to positive (+) 5 kV. Within the signal to noise of our sum frequency instrument, this implies negligible change of the orientation of the dangling OH under current experimental conditions.

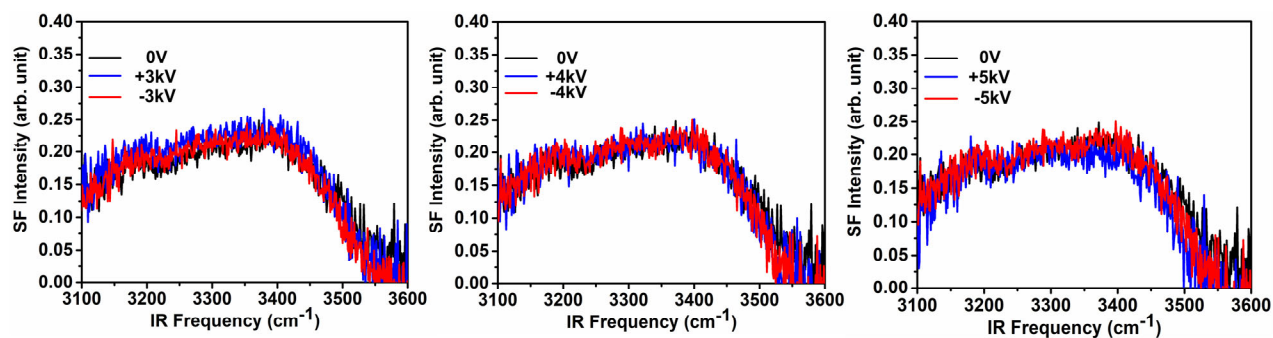


Fig. S5. The vibrational sum frequency generation spectra of the neat water-air interface in the hydrogen-bonded OH stretching region with ssp polarization combination under applied external potential. The polarizations are listed in the order of decreasing frequency from left to right (sum frequency, visible, IR). The black, blue and red colors are the sum frequency spectra under unbiased (0 V), positive and negative applied potential, respectively. Minimal change to the sum frequency response is noted (each plot should be compared within itself for intensity variations). The data for H-bonded OH region were obtained with 60 seconds integration time with 5 averages, and plotted after background subtraction and normalization with respect to non-resonant signal from a gold mirror. The measured sum frequency spectra show no appreciable change under applied external potential in the range of negative (-) 5 kV to positive (+) 5 kV. Within the signal to noise of our sum frequency instrument, this implies negligible or very small changes of the hydrogen bond network under current experimental conditions.

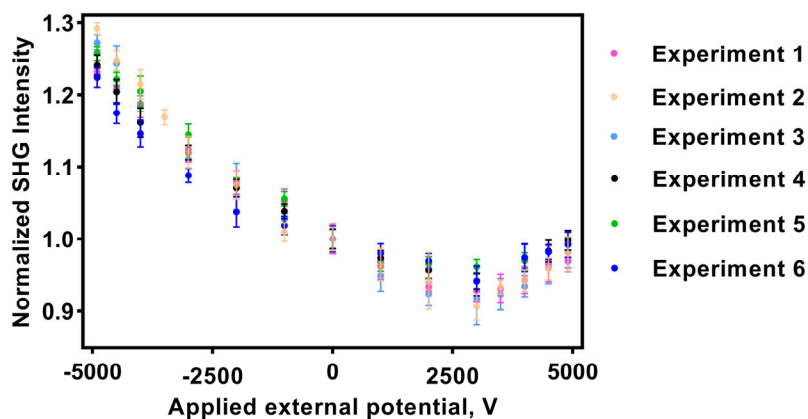


Fig. S6. Experimental reproducibility under (P in P out polarization). The second harmonic intensities of neat water surface at different external potential are normalized to the neat zero bias response. Here, the pink, yellow, sky blue, black, green, and blue colors indicate the average second harmonic intensity with one standard deviation of the experiment 1, 2, 3, 4, 5 and 6, respectively.

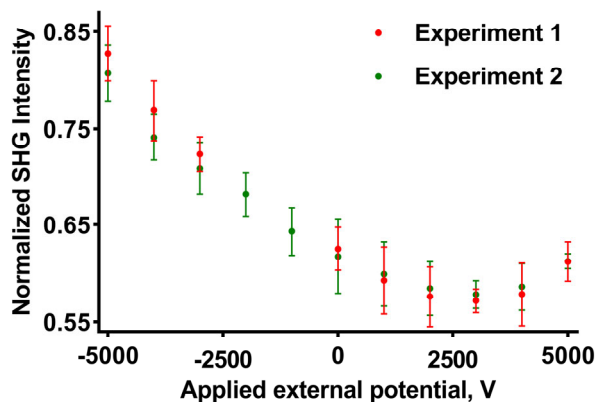


Fig. S7. Experimental reproducibility (45 in with S out polarization). The second harmonic intensities of neat water surface at different external potential are normalized to the neat zero bias response. Here, the red and green colors indicate the average second harmonic intensity with one standard deviation of the experiment 1 and 2, respectively.

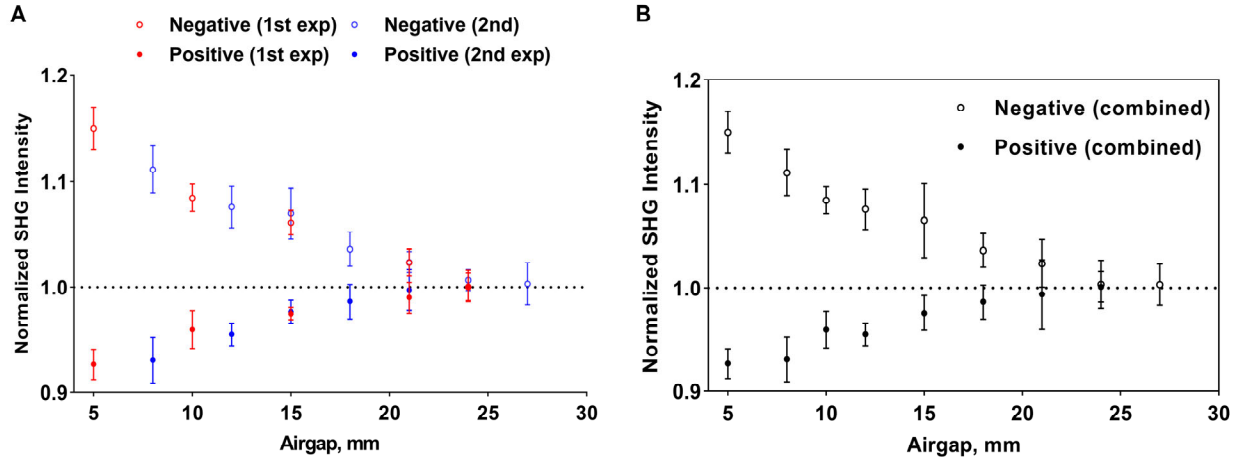


Fig. S8. Airgap test (P in P out polarization). The normalized second harmonic intensities of the neat water-air interface with the change in airgap between water interface to air-electrode at 3 kV external potential. The airgap spans from 0.5 cm to 2.7 cm. A) The red and blue colors indicate second harmonic responses of first and second experiments, respectively. Also, the open and close circles indicate average second harmonic responses applying negative and positive external potential, respectively, with one standard deviation. B) The open and closed black circles indicate average second harmonic responses (combined first and second experiments) applying negative and positive external potentials, respectively, with one standard deviation.

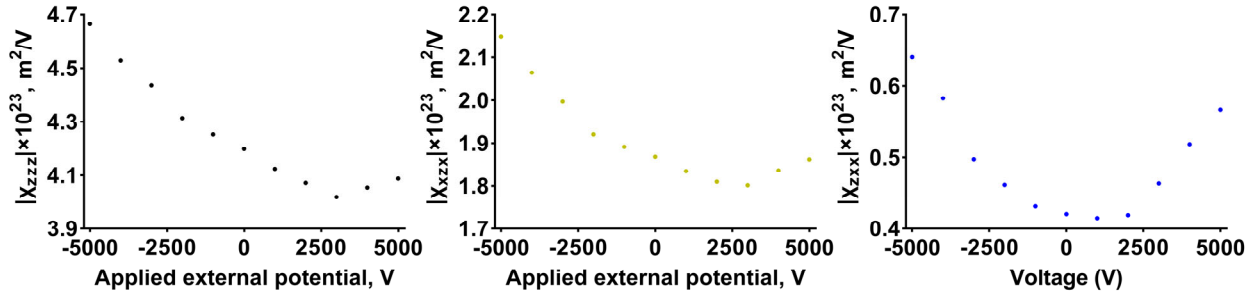


Fig. S9. The Fresnel-removed second order susceptibilities of neat water surface at different external potential and polarization. Here, the black, yellow, and blue colors indicate the Fresnel-removed second order susceptibilities of neat water surface at P in P out, 45 in with S out and S in P out polarization, respectively.

2. Discussion of SH power calculation

The average SH power, $P_{2\omega, avg}$, is calculated with the equation below:

$$P_{2\omega, avg} = C_{ps} E_{2\omega} t_{ins} = C_{ps} h \nu_{2\omega} t_{ins} = C_{ps} h \frac{c}{\lambda_{2\omega}} t_{ins} \quad (S1)$$

Where C_{ps} , $E_{2\omega}$ and t_{ins} are the photon counts of detected SH photons on CCD with a unit of counts per second, energy of photon with the unit of Joule and instrumental transmission function that compensates the loss of photons by optics and electronics from the detector, respectively. Table S2 shows the parameters within instrumental transmission function in percentage or ratio. The calculation of t_{ins} is shown below using the reported parameters in Table S2:

$$t_{ins} = \frac{1}{70\%} \times \frac{1}{64\%} \times \frac{1}{57\%} \times \frac{1}{200} \times 1 = 0.01958$$

3. Calculation of effective second order susceptibility $\chi_{eff}^{(2)}$:

The equation of the second harmonic electric field, $E_{2\omega}$, follows the expression by Mizrahi et al., Shen et al. and Woodward et al. with some modification for SI unit calculation:⁷⁻⁹

$$E_{2\omega} = \frac{(2\omega) \sec \theta}{2nc} \left| \chi_{s, eff}^{(2)} \right| E_{\omega}^2 \quad (S2)$$

Where ω is the angular frequency of fundamental light (805 nm), θ is either incident angle of fundamental or SH reflected angle from the surface ($\theta = \theta_{in} = \theta_{out} = 68.2^\circ$), n is the refractive index of air ($n = n_{\omega} = n_{2\omega} = 1$), c is the speed of light, E_{ω} is the electric field of the fundamental light.

In order to substitute the equation with experimental parameters, the above equation is squared and expressed in the form of intensity:

$$E_{2\omega}^2 = \left(\frac{\omega \sec \theta}{nc} \right)^2 \left| \chi_{s, eff}^{(2)} \right|^2 E_{\omega}^4 \quad (S3)$$

The intensity is substituted with $I = \frac{1}{2} \epsilon_0 n c E^2$:

$$I_{2\omega, pk} = \frac{2\omega^2 \sec^2 \theta}{\epsilon_0 n^3 c^3} \left| \chi_{s, eff}^{(2)} \right|^2 I_{\omega, pk}^2 \quad (S4)$$

Here, $I_{i, pk}$ and ϵ_0 are the peak intensity of light ($i = 2\omega$ or ω) and vacuum permittivity, respectively. Further we convert the peak intensity to average intensity and average power:

$$I_{i, pk} = \frac{I_{i, avg}}{f\tau} = \frac{P_{i, avg}}{f\tau A_i} = \frac{P_{i, avg}}{f\tau(\pi r_i^2)} \quad (S5)$$

Here, $I_{i, avg}$ is the average intensity of the light ($i = 2\omega$ or ω). f and τ represent the repetition rate (82 MHz) and the pulse width of laser (50 fs), respectively. A_i is the area of the beam spot of SH and fundamental laser with the unit of m^2 . Since the radius of SH light is $\sqrt{2}$ smaller than the radius of

fundamental light, the overall area of SH spot is half of the fundamental focused spot.¹⁰ Thus, the equation can be rewrite as:

$$P_{2\omega,avg} = \frac{\omega^2 \sec^2 \theta}{\epsilon_0 n^3 c^3 f \tau (\pi r_\omega^2)} \left| \chi_{s,eff}^{(2)} \right|^2 P_{\omega,avg}^2 \quad (S6)$$

$P_{\omega,avg}$ is measured average power of the fundamental laser in the unit of Watt. We obtain the below equation by substitution of equation (S6) into equation (S1):

$$C_{ps} h \frac{c}{\lambda_{2\omega}} t_{ins} = \frac{\omega^2 \sec^2 \theta}{\epsilon_0 n^3 c^3 f \tau (\pi r_\omega^2)} \left| \chi_{s,eff}^{(2)} \right|^2 P_{\omega,avg}^2 \quad (S7)$$

The Fresnel-removed effective second order susceptibilities can be obtained by applying the Fresnel factors with the combination of specific light polarization:¹¹

$$\chi_{eff,SP}^{(2)} = L_{2\omega,zz} [L_{\omega,yy}]^2 \sin \theta \chi_{zyy} \quad (S8)$$

$$\chi_{eff,45S}^{(2)} = L_{2\omega,yy} L_{\omega,zz} L_{\omega,yy} \sin \theta_{2\omega} \chi_{yzy} \quad (S9)$$

$$\begin{aligned} \chi_{eff,PP}^{(2)} = & L_{2\omega,zz} [L_{\omega,xx}]^2 \sin \theta \cos^2 \theta_{2\omega} \chi_{zxx} - 2 L_{2\omega,xx} L_{\omega,zz} L_{\omega,xx} \cos \theta \sin \theta_{2\omega} \cos \theta_{2\omega} \chi_{xzx} \\ & + L_{2\omega,zz} [L_{\omega,zz}]^2 \sin \theta \sin^2 \theta_{2\omega} \chi_{zzz} \end{aligned} \quad (S10)$$

Where θ is the incident angle of the fundamental and $\theta_{2\omega}$ is the reflected angle of SH light from surface normal. Here, $L_{i,xx}$, $L_{i,yy}$ and $L_{i,zz}$ are Fresnel factors shown below:

$$L_{i,xx} = \frac{2n_{i,1} \cos \gamma}{n_{i,1} \cos \gamma + n_{i,2} \cos \theta} \quad (S11)$$

$$L_{i,yy} = \frac{2n_{i,1} \cos \theta}{n_{i,1} \cos \theta + n_{i,2} \cos \gamma} \quad (S12)$$

$$L_{i,zz} = \frac{2n_{i,2} \cos \theta}{n_{i,1} \cos \gamma + n_{i,2} \cos \theta} \left(\frac{n_{i,1}}{n'_i} \right)^2 \quad (S13)$$

In the Fresnel factor equations (S11, S12 and S13), $n_{i,1}$ and $n_{i,2}$ are the refractive indices of medium 1 (air) and medium 2 (water), respectively. γ is the refracted angle of the incident light in medium 2. n'_i is the refractive index of interfacial layer, where we use the value $n'_i = 1.15$ for the air-water interface.⁴

4. Supplementary Tables:

Table S1. The pH of neat water on different days of the experiment. Variation between before and after experiment is due to equilibration of the water samples with atmospheric background of carbon dioxide, consistent with lab air exposure.

Experiments	pH (before the experiment)	pH (after the experiment)
1	6.19±0.01	5.86±0.01
2	6.26±0.01	5.89±0.01
3	6.29±0.01	5.90±0.01
4	6.34±0.02	5.76±0.02
5	6.32±0.01	5.69±0.02
6	6.31±0.01	5.72±0.01

Table S2. Parameters of optics and electronics in the instrumental transmission function.

Optics and electronics	Transmittance or ratio
Optics	70%
Grating	64%
Quantum efficiency of CCD	57%
EM gain	200x
Preamplifier	1x

References

1. Feng, R.-R.; Guo, Y.; Wang, H.-F., Reorientation of the "free OH" group in the top-most layer of air/water interface of sodium fluoride aqueous solution probed with sum-frequency generation vibrational spectroscopy. *J. Chem. Phys.* **2014**, *141* (18), 18C507/1-18C507/10.
2. Gan, W.; Wu, D.; Zhang, Z.; Feng, R.-r.; Wang, H.-f., Polarization and experimental configuration analyses of sum frequency generation vibrational spectra, structure, and orientational motion of the air/water interface. *J. Chem. Phys.* **2006**, *124* (11), 114705/1-114705/15.
3. Adams, E. M.; Verreault, D.; Jayarathne, T.; Cochran, R. E.; Stone, E. A.; Allen, H. C., Surface organization of a DPPC monolayer on concentrated SrCl₂ and ZnCl₂ solutions. *Phys. Chem. Chem. Phys.* **2016**, *18* (47), 32345-32357.
4. Adams, E. M.; Wellen, B. A.; Thiriaux, R.; Reddy, S. K.; Vidalis, A. S.; Paesani, F.; Allen, H. C., Sodium-carboxylate contact ion pair formation induces stabilization of palmitic acid monolayers at high pH. *Phys Chem Chem Phys* **2017**, *19* (16), 10481-10490.
5. Lin, L.; Husek, J.; Biswas, S.; Baumler, S. M.; Adel, T.; Ng, K. C.; Baker, L. R.; Allen, H. C., Iron(III) Speciation Observed at Aqueous and Glycerol Surfaces: Vibrational Sum Frequency and X-ray. *J. Am. Chem. Soc.* **2019**, *141* (34), 13525-13535.
6. Conboy, J. C.; Messmer, M. C.; Richmond, G. L., Investigation of Surfactant Conformation and Order at the Liquid-Liquid Interface by Total Internal Reflection Sum-Frequency Vibrational Spectroscopy. *J. Phys. Chem.* **1996**, *100* (18), 7617-22.
7. Mizrahi, V.; Sipe, J. E., Phenomenological treatment of surface second-harmonic generation. *J. Opt. Soc. Am. B: Opt. Phys.* **1988**, *5* (3), 660-7.
8. Shen, Y. R., Optical second harmonic generation at interfaces. *Annu. Rev. Phys. Chem.* **1989**, *40*, 327-50.
9. Woodward, R. I.; Murray, R. T.; Phelan, C. F.; De Oliveira, R. E. P.; Runcorn, T. H.; Kelleher, E. J. R.; Li, S.; De Oliveira, E. C.; Fehine, G. J. M.; Eda, G.; De Matos, C. J. S., Characterization of the second- and third-order nonlinear optical susceptibilities of monolayer MoS₂ using multiphoton microscopy. *2D Mater.* **2017**, *4* (1), 011006/1-011006/7.
10. Geiger, F. In *Beyond the Gouy-Chapman model with heterodyne-detected second harmonic generation*, American Chemical Society: 2019; pp PHYS-0199.
11. Zhuang, X.; Miranda, P. B.; Kim, D.; Shen, Y. R., Mapping molecular orientation and conformation at interfaces by surface nonlinear optics. *Physical Review B* **1999**, *59* (19), 12632.